Riemannian space tessellation with polyhedral room images

Jean-Dominique Polack, Aidan Meacham, Roland Badeau, Jean-Christophe Valière

Riemannian space tessellation with polyhedral room images

Jean-Dominique Polack[a], Aidan Meacham[b], Roland Badeau[c], Jean-Christophe Valière[d]

a. Institut Jean Le Rond D'Alembert (IJLRA), Sorbonne Université, CNRS UMR 7190, France
jean-dominique.polack@sorbonne-universite.fr
b. Institut Jean Le Rond D'Alembert (IJLRA), Sorbonne Université, CNRS UMR 7190, France
aidan.meacham@sorbonne-universite.fr
c. LTCI, Télécom Paris, Institut Polytechnique de Paris, France
roland.badeau@telecom-paris.fr
d. Institut PPRIME, Université de Poitiers, CNRS UPR3346, France jean.christophe.valiere@univ-poitiers.fr

March 4, 2022

Abstract

We show that Riemannian geometry is the natural setting for developing polyhedral rooms of arbitrary shapes into their image rooms, and therefore counting the image sources. This new setting makes it also possible to account for scattering on particular edges, called hinges, characterized by negative deficit dihedral angles created by reflections on the adjacent faces. Using energy conservation, we show that sound rays are then deviated by the hinges, depending on their frequencies and the distances they pass by.

Keywords: Riemannian geometry, polyhedral rooms, scattering, stress-energy tensor, room acoustic modelling.

1 Introduction

Computing the number of image sources for a rectangular enclosure is an easy task that acousticians routinely carry out [CM78]. Indeed, as all the images of the room tesselate the Euclidean space, the computation simply amounts to dividing the volume of a sphere of radius ct, where c is the speed of sound and t the time elapsed since the source emited, by the volume of the original room, as each image room, or cell, only contains one image source. Thus one obtains a number of image sources that increases with the square of the time elapsed since the source emitted and is inversely proportional to the volume of the room, and most acousticians consider that this approximation is also

valid for rooms of arbitrary shapes. As a consequence, most simulation codes routinely use the mean number of image sources for rectangular rooms when they fix the complexity of the algorithms that compute the late reverberation, independently of the actual room shape [NE93].

Few authors have questionned the validity of this approximation for rooms of arbitrary shapes. [Pol92] has argued that this number should increase exponentially for mixing rooms, as a consequence of the conservation of the phase space measure. Indeed, in mixing rooms, any small volume of the phase space, for example the initial volume around the source, exponentially expands in at least one phase dimension as it propagates with time, and exponentially decreases in at least one dimension, so that any volume decays into exponentially thin stripes. Any elementary cell of the phase space thus intersects exponentially many stripes, corresponding to exponentially many image sources.

Polyhedral rooms, on the other hand, are not mixing rooms since two neighbouring rays in the phase space almost certainly separate linearly with time, and not exponentially. Thus, the preceding argument cannot be used to evaluate the number of image sources. The present paper therefore addresses the non trivial issue of computing the number of images sources for arbitrary polyhedral enclosures. It first examines the reflection and scattering on non rectangular dihedral angles and shows that successive reflections on the adjacent faces always add up to a total angle in excess of 2π, so that taking into account reflections on all the faces of a polyhedron leads to the tessellation of a Riemaniann space with negative curvature where edges take the role of the "hinges" of Regge's discretization of Riemannian spaces [Reg61]. Afterwards, it moves to computing the number of image sources, and proposes a computational scheme based on the number of faces, edges and vertices, that is, the isometry group of the space. Then, it addresses the question of the visible image sources that are linked with the receiver by rays that do not cross any edge of image rooms, and derives from it the notion of visible horizon. Finally, scattering is taken into account by introducing the wave nature of the sound field in a room, and the conservation of its energy and intensity.

2 Scattering on non rectangular dihedral angles

The proper setting for computing scattering on non rectangular dihedral angles is Riemannian geometry. We therefore first expose the principles of this geometry and the properties of its metric tensor.

2.1 Riemannian geometry

We consider an n-dimensional space with its positive-definite metric tensor g_{ij} and the volume element $dV = \sqrt{g}dx^1 \dots dx^n$, where $g = \det g_{ij}$ is positive [Lin 5]. The infinitesimal distance element is given by:

$$ds^2 = g_{ij}dx^i dx^j \tag{1}$$

and we note g^{ij} the inverse matrix of g_{ij}. ∇_i is the covariant derivation with respect to x^i, which differs from the usual partial derivation ∂_i in a way that depends on the tensor rank. For example, for a function Φ:

$$\nabla_j \Phi = \partial_j \Phi = \Phi_j$$

but $\nabla_j \Phi_i = \partial_j \Phi_i - \Gamma^k_{ji} \Phi_k$ and $\nabla_j X^i = \partial_j X^i + \Gamma^i_{jk} X^k$, where X^i are the (contravariant) components of vector X and Γ^k_{ji} the Christoffel symbols linked to the derivatives of the elements of the metric tensor g_{ij}:

$$\Gamma^k_{ji} = \frac{1}{2} g^{kl} \left(\partial_j g_{il} + \partial_i g_{lj} - \partial_l g_{ji} \right) \tag{2}$$

Note that, unlike ordinary differentiations, covariant derivations do not commute. Their commutators is given by the curvature of the time-space [Lin 5]:

$$\left(\nabla_i \nabla_j - \nabla_j \nabla_i \right) X^k = R^k_{mij} X^m \tag{3}$$

where the R^k_{mij} are the elements of the Riemann tensor. However, for a function, $\nabla_i \partial_j \Phi = \nabla_j \partial_i \Phi$; and by construction, all covariant derivatives of the elements of the metric tensor are null. In other words, the contravariant derivation ∇^i is defined by:

$$\nabla^i = g^{ij} \nabla_j = \nabla_j g^{ij}$$

One calls *vectors* tensors with one upper index, such as X^i; and *covectors* tensors with one lower index, such as Φ_i.

The Ricci curvature tensor can be computed from the derivative of the Christoffel symbols, by contraction of the Riemann curvature tensor on two indices. One obtains successively:

- the Riemann tensor: $R^l_{kij} = \partial_i \Gamma^l_{jk} - \partial_j \Gamma^l_{ik} + \Gamma^m_{jk} \Gamma^l_{im} - \Gamma^m_{ik} \Gamma^l_{jm}$
- the Ricci tensor: $R_{ij} = R^l_{ilj}$
- the scalar curvature: $R = g^{ij} R_{ij}$; and the local curvature is obtained by integrating half the scalar curvature over a small space element, that is, $\frac{1}{2} \int R \sqrt{g} dx^1 \dots dx^n$

In this Section and the following one, we shall only consider 2- and 3-dimensional Riemannian spaces, which are embedded in 3- or 4-dimensional Euclidean spaces in order to derive the metric tensor.

2.2 2-dimensional scattering on obtuse angles

We first consider the obtuse angle β of Fig. 1 in a 2-dimensional Euclidean space. A sound source S (black star) emitting inside the angle emits rays in all directions. Some rays impinge on the left arm Ox of the angle and are reflected (red arrows). As the position of impact moves clockwise toward the apex, the reflected ray gradually moves upwards and eventually hits the right arm on which it is reflected once more. Finally, the ray impacts the apex of the angle (black upwards broken-line arrow).

In a similar fashion, some rays will impinge on the right arm Oy and be reflected (green arrows). As the position of impact moves anticlockwise toward the apex, the reflected ray gradually moves upwards and eventually hits the left arm on which it is reflected once more. Despite the continuity of the impinging rays around the apex, there is no continuity of the reflected rays, and this creates scattering.

In order to visualise the scattering, one needs to consider the images of the sources by reflection on the two arms of the angle. Let's call S'_l the image

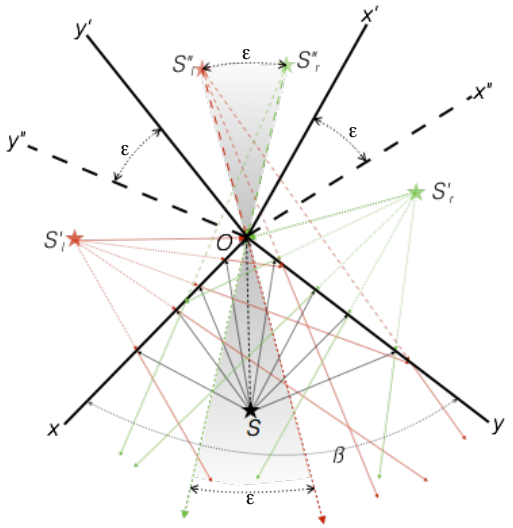

Figure 1: Reflection and scattering of sound rays on obtuse angle β. ε is the excess angle, since second order image angles overlap by ε.

of the source on the left arm (red star), and S'_r the image on the right arm (green star); S''_l the left-most second order image (dim red star), and S''_r the right-most second order image (dim green star). Reflected rays on the arms of the angle are first emitted from the first order image sources S'_l and S'_r, then from the second order sources S''_l and S''_r when the reflected rays hit the opposite arm, until the rays emitted from the first-order image sources reach the apex (red and green dotted-line arrows). In that position, the rays emitted from the second order image sources do not coincide in direction, since they are emitted from two different image sources at angle ε with respect to the apex. Scattering therefore comes in to *fill the gap* between these two directions, and in fact beyond them. In other words, one must consider a continuum of image sources along the sector between S''_l and S''_r (grey sector), that is, one must rotate the second order image angle by ε from position $y''0x'$ to position $y'0x''$.

In fact, when rays rotate *clockwise* around the original source S, the reflected rays rotate *anticlockwise* around the first order source S''_l, and *clockwise* around the second order source S''_r. So, when the secondary source moves *clockwise* from S''_l to S''_r on Fig. 1, the diffracted rays rotate *clockwise* around the apex, thus filling the grey sector with continuity of rotations at its boundaries.

In order to make the second order image angles coincide, one needs to embed Fig. 1 in a 3-dimensional space as in Fig. 2. We call x_1, y_1, and z_1 the three Cartesian coordinates, and keep notations Ox and Oy for the arms of the original flat angular sector, which is now slanted so that angle β exactly projects on a right angle. As a consequence, Ox is elevated by angle α above Ox_1 and Oy is lowered by angle α below Oy_1; similarly, $O(-x)$ is elevated by angle α above $O(-x_1)$ and $O(-y)$ is lowered by angle α below $O(-y_1)$, so that the apex angle remains equal to β. In such a way, we obtain a *locally flat* space where rays are free to cross the borders between subsequent angular sectors without changing their direction. Further, the embedding makes it possible to define the metric

tensor of this space.

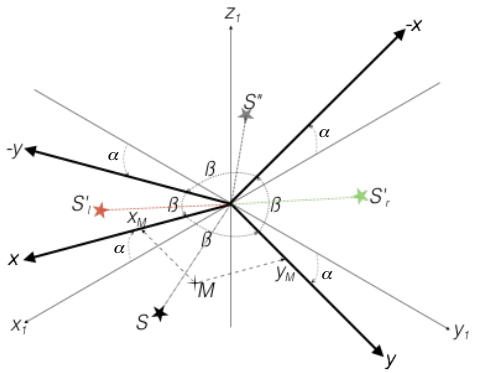

Figure 2: Embedding scattering on obtuse angle in 3-dimensional space. Angles α are vertical and measure deviations of angle arms from horizontal plane. Note that the two second order image sources coalesce in one single image source.

When the angle α is not null, that is, when $\beta > \frac{\pi}{2}$, the position of any point M in the system is given by its coordinates x and y, that are no longer orthogonal. In order to compute the corresponding infinitesimal distance element, one must project coordinates x and y on the Ox_1y_1 plane, then compute the vertical coordinate with equation:

$$z_1 = \tan\alpha(\mid x_1 \mid - \mid y_1 \mid)$$

valid for the four sectors of the system. With the convention $\mathrm{sgn}(0) = 0$, one obtains everywhere, even on the arms of the angles:

$$\begin{aligned} ds^2 &= dx_1^2 + dy_1^2 + dz_1^2 \\ &= (1+\tan^2\alpha)dx_1^2 + (1+\tan^2\alpha)dy_1^2 - 2\mathrm{sgn}(x)\mathrm{sgn}(y)\tan^2\alpha dx_1 dy_1 \end{aligned}$$

with $dx = \sqrt{1+\tan^2\alpha}dx_1$ and $dy = \sqrt{1+\tan^2\alpha}dy_1$, that is:

$$\begin{aligned} ds^2 &= dx^2 + dy^2 - 2\mathrm{sgn}(x)\mathrm{sgn}(y)\frac{\tan^2\alpha}{1+\tan^2\alpha}dxdy \\ &= dx^2 + dy^2 - 2\mathrm{sgn}(x)\mathrm{sgn}(y)\sin^2\alpha\, dxdy \end{aligned}$$

Simple projection on the plane Ox_1y_1 shows that $-\sin^2\alpha = \cos\beta$. Note that $\cos\beta < 0$ since $\frac{\pi}{2} < \beta < \pi$ for obtuse angles. The last equation can therefore be written as:

$$ds^2 = dx^2 + dy^2 + 2\mathrm{sgn}(x)\mathrm{sgn}(y)\cos\beta\, dxdy \tag{4}$$

Using the embedding in the 3-dimensional space, distance elements ds are obviously continuous along a line that crosses one of the arms, implying that dx and dy are modified when the line crosses the arms. From the expression of ds^2, it is easy to deduce the metric tensor, its inverse, and its determinant:

$$g_{ij} = \begin{pmatrix} 1 & \mathrm{sgn}(x)\mathrm{sgn}(y)\cos\beta \\ \mathrm{sgn}(x)\mathrm{sgn}(y)\cos\beta & 1 \end{pmatrix} \tag{5}$$

$$g^{ij} = \frac{1}{\sin^2\beta}\begin{pmatrix} 1 & -\mathrm{sgn}(x)\mathrm{sgn}(y)\cos\beta \\ -\mathrm{sgn}(x)\mathrm{sgn}(y)\cos\beta & 1 \end{pmatrix}$$
$$g = \sin^2\beta \tag{6}$$

Note that g_{ij} and g^{ij} reduce to the identity matrix on the arms ($x = 0$ or $y = 0$) because of the convention $\mathrm{sgn}(0) = 0$, with $g = 1$.

Successive derivations lead to:

- the Christoffel symbols are all equal to 0, but for:

$$\begin{aligned} \Gamma^y_{xx} &= g^{yy}\partial_x g_{xy} = 2\delta(x)\mathrm{sgn}(y)\cos\beta \\ \Gamma^x_{yy} &= g^{xx}\partial_y g_{xy} = 2\mathrm{sgn}(x)\delta(y)\cos\beta \end{aligned} \tag{7}$$

  where δ is the Dirac distribution, and where we have used the form for g^{xy} valid on the arms because $\delta(x)$, resp. $\delta(y)$, is null everywhere except on the arms $x = 0$, resp. $y = 0$;

- the Ricci tensor has elements:

$$\begin{aligned} R_{xx} &= R_{yy} = 4\delta(x)\delta(y)\cos\beta \\ R_{xy} &= R_{yx} = 0 \end{aligned} \tag{8}$$

- the scalar curvature and the local curvature are resp. $R = 8\delta(x)\delta(y)\cos\beta < 0$ and $\frac{1}{2}\int R\sqrt{g}dxdy$.

It is easy to see that the curvature is null everywhere but at the apex O where it is equal to $4\cos\beta$, which tends toward $4(\frac{\pi}{2} - \beta)$ for small values of $\frac{\pi}{2} - \beta$. Indeed, Regge [Reg61] has shown that the curvature is equal to the total deficit angle at the apex $-\varepsilon = 2\pi - 4\beta$.

2.3 3-dimensional scattering on obtuse dihedral angles

For a 3-dimensional obtuse dihedral angle, Fig 1 represents a projection of the rays on a plane perpendicular to the apical edge. But no equivalent of Fig 2 can be drawn, as the embedding takes place in a 4-dimensional space.

Introducing a new coordinate z, perpendicular to the two coordinates x and y of the Riemannian plane of Fig 2, the infinitesimal distance element (4) must now be completed into:

$$ds^2 = dx^2 + dy^2 + dz^2 + 2\mathrm{sgn}(x)\mathrm{sgn}(y)\cos\beta\, dxdy \tag{9}$$

with the metric tensor and its inverse now given by

$$g_{ij} = \begin{pmatrix} 1 & \mathrm{sgn}(x)\mathrm{sgn}(y)\cos\beta & 0 \\ \mathrm{sgn}(x)\mathrm{sgn}(y)\cos\beta & 1 & 0 \\ 0 & 0 & 1 \end{pmatrix} \tag{10}$$

$$g^{ij} = \frac{1}{\sin^2\beta}\begin{pmatrix} 1 & -\mathrm{sgn}(x)\mathrm{sgn}(y)\cos\beta & 0 \\ -\mathrm{sgn}(x)\mathrm{sgn}(y)\cos\beta & 1 & 0 \\ 0 & 0 & \sin^2\beta \end{pmatrix}$$

with determinant g still given by (6); and g_{ij} and g^{ij} reduce to identity matrices on the planes $x = 0$ and $y = 0$, which we still call arms, with $g = 1$. All

Christoffel symbols are equal to 0 but Γ^y_{xx} and Γ^x_{yy} still given by eq. (7), and all elements of the Ricci tensor are 0 except $R_{xx} = R_{yy}$ still given by eq. (8). The scalar curvature therefore remains $R = 8\delta(x)\delta(y)\cos\beta < 0$, but the local curvature, obtained by integrating half the scalar curvature over a small space element, is now equal to $\frac{1}{2}\int R\sqrt{g}dxdydz$. It remains null everywhere - flat space - except on the apical edge. In the limit where β tends toward a right angle, the curvature around the apical edge is equal to $(2\pi - 4\beta)\ell$, where ℓ is the length of the apical edge, called *hinge* by [Reg61]. Note that hinges are subspaces of co-dimension 2 where excess angle is non null.

2.4 Scattering on reflex angles

The case of a reflex angle, both in 2 and 3 dimensions (see Fig. 3) can be handled in a similar fashion. But in this case, we only need to consider the first order images of the angle to obtain excess angles at the apex, and rays are never reflected twice.

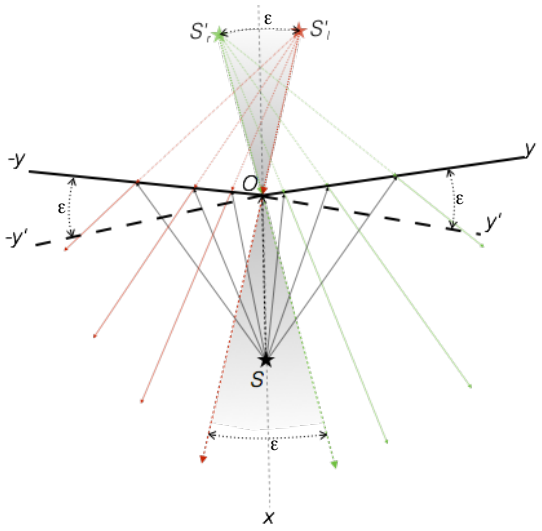

Figure 3: Reflection and scattering of sound rays on reflex angle. ε is the excess angle, since image angles overlap by ε.

As for obtuse angle, when rays rotate *clockwise* around the source, the reflected rays rotate *anticlockwise*, first around the image source S'_l, then around S'_r. In order to fill the gap at the apex, the image source must move *anticlockwise* from S'_l to S'_r. It can be seen on Fig. 3 that the diffracted rays then rotate *anticlockwise* around the apex, thus filling the grey sector with continuity of rotations at its boundaries. One considers again a continuum of image sources along the sector between S'_l and S'_r (grey sector) by rotating the image angle by ε, from position $(-y)Oy'$ to position $(-y')Oy$.

Introducing the axis Ox along the bisector of the reflex angle, Fig. 3 (2-dimensional case) can still be embedded in a 3-dimensional space, as displayed in Fig. 4. The notations are the same as in Sect. 2.2 and 2.3 for the 2-dimensional and 3-dimensional cases respectively. As a consequence, curvatures only occur

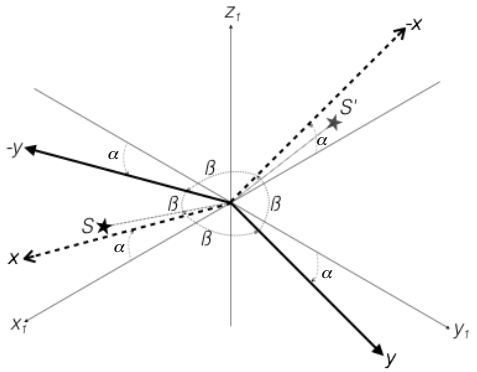

Figure 4: Embedding scattering on reflex angle in 3-dimensional space. Axis Ox is introduced as the bisector of the angle. Angles α and β have the same meaning as in Figs. 1 and 2. This time, the two first order image sources coalesce in one single image source S'.

on the "hinge" and keep the same values, and so do the metric tensors, the Christoffel symbols, and the Ricci tensors.

Note that only one image angle is created by scattering on a reflex angle, making them similar to flat edges or faces, except for the curvature localized on the hinges and the corresponding scattering.

2.5 Scattering on acute angles

The construction of Figs. 1 and 2 can easily be extended to any acute angle. In this case, the number of image angles must be increased, while keeping it odd, until one obtains an excess apical angle (see Fig. 5).

As for the two previous cases, when rays rotate *clockwise* around the original source, the reflected rays rotate *anticlockwise* around the first order image source S'_r, then *clockwise* around he second order source S''_l until the reflected ray reaches the apex. Continuity of rotation requires that this second order image source rotates *clockwise*, but it does not fill the gap between the two second order sources: image source S''_l moves away from S''_r until it reaches a second position, marked with a red broken line in the bottom panel of Fig. 5, at which further rotation makes it disappear. However, just before it disappears, a *third order* image source S''', not represented in the bottom panel of Fig. 5, emerges on the left. This third order image source fills the whole angle with diffracted rays while it keeps on rotating *clockwise* around the apex, until it disappears to the right. Shortly afterwards, the second order image source S''_r appears on the left at the position marked with the green broken line, and further *clockwise* rotation brings it to its original position in the top panel. Thus, this time, the diffracted rays fill the whole angle, plus the two sectors outside the grey sector on Fig. 5.

In order to correctly embed scattering on an acute angle in a 3-dimensional space, adapted sets of coordinates must be introduced; but curvature remains localized at the apical hinge and is equal to the deficit angle $-\varepsilon$ (not represented in Fig. 5), time the length of the hinge in the dihedral case. In fact, since the

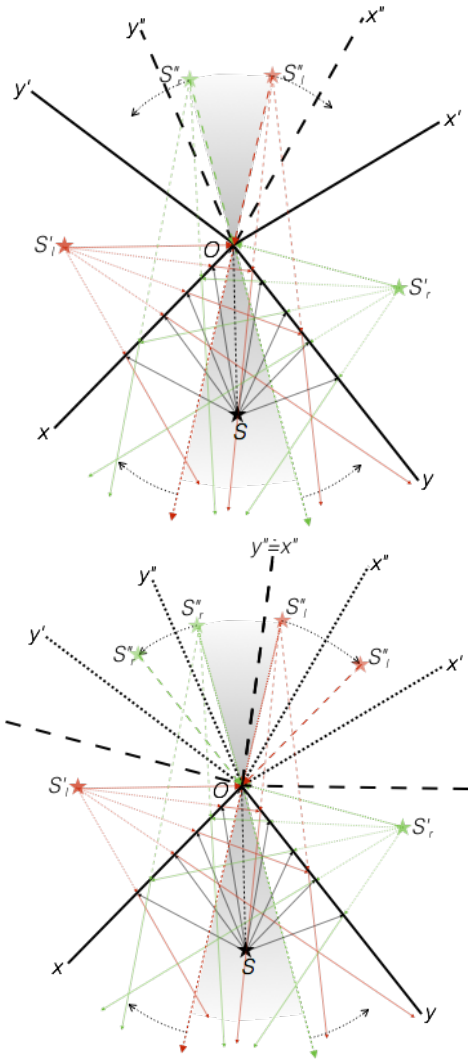

Figure 5: Reflection and scattering of sound rays on acute angle. Top: the visible rays; bottom: rotating S''_l clockwise makes a supplementary image source S''' appear and fill in the whole angle with diffracted rays (not represented), until S''_r eventually becomes visible on the left hand side. Note that for some positions no image source diffracts in the angle, whilst two sources can simultaneously diffract for some other positions.

space is Euclidean everywhere but on the apex, any directions can be chosen, provided that the angle between them is equal to $\frac{\pi}{2} - \frac{\varepsilon}{4} = \beta$. In Fig 6, the angle is located in the front sector, and its 5 images are displayed around the hinge O.

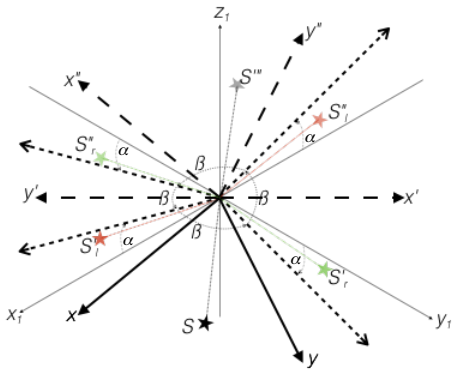

Figure 6: Embedding scattering on acute angle in 3-dimensional space. Short-tick axes represent the original axes of the warped plan; acute angle is inserted in the front sector. Angles α and β have same meanings as in previous Figures. The third order image sources coalesce in one single image source S'''.

Scattering is now created by the non overlapping highest order image sources radiating through the hinge.

3 Number of image sources

Let us now consider polygonal (2-dimensional case) or polyhedral rooms (3-dimensional case). We impose the restriction, that will be discussed at the end of this Section, that all the internal angles of the polygons are right or obtuse in order to obtain the 4 sectors of Figs. 1 and 2. In the polyhedral case, beside keeping all internal dihedral angles right or obtuse for the same reason, we also impose that all vertices are shared by three faces only. Typical examples are pentagons in 2-dimensions, and dodecahedra in 3-dimensions.

3.1 Convex polygonal rooms

For convex polygonal rooms with n edges, the n first order images are obtained by reflection on the edges. However, the order of reflection is not relevant for counting the images: layers are much more relevant. Thus, on Fig. 7, the numbers correspond to the successive layers around the original room.

Accordingly, the first layer is composed of the n images on the edges, to which n supplementary images, one at each vertex, are added. For the next layers, it is more efficient to compute separately the number of free edges and the number of free vertices, that is, edges and vertices that are not common to two adjacent images: one adds one image for each free edge, and one for each free vertex, exactly as for the first layer. It can be seen on Fig. 7 that edge images create $(n-3)$ free edges and $(n-4)$ free vertices; and vertex images

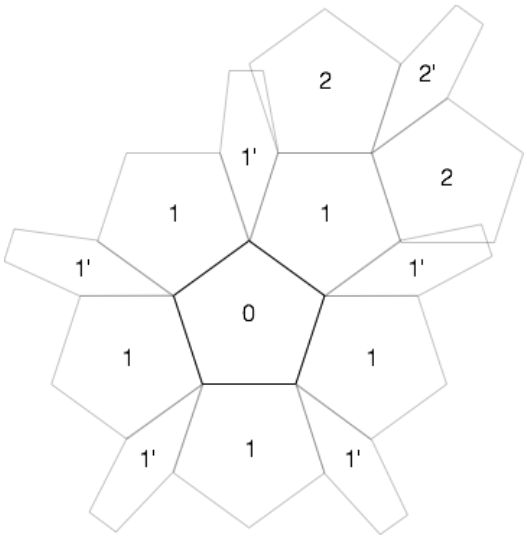

Figure 7: Image rooms of pentagon. Primed images are skewed in order to fit in the picture. Numbers correspond to successive layers of images, with 0 denoting the original room and primes one supplementary order of reflection (see text). Note that one supplementary image must be added each time image rooms overlap (e.g. between 1′and 2).

crate $(n-2)$ free edges and $(n-3)$ free vertices. Note that $n \geqslant 4$ if all angles are right or obtuse. Let's call e_i the number of free edges and v_i the number of free vertices of layer i. One obtains the recurrence formula:

$$\begin{pmatrix} e_i \\ v_i \end{pmatrix} = \begin{pmatrix} n-3 & n-2 \\ n-4 & n-3 \end{pmatrix} \begin{pmatrix} e_{i-1} \\ v_{i-1} \end{pmatrix} = \Lambda^i \begin{pmatrix} e_0 \\ v_0 \end{pmatrix} \tag{11}$$

where $\Lambda = \begin{pmatrix} n-3 & n-2 \\ n-4 & n-3 \end{pmatrix}$ and $\det \Lambda = 1$. The eigenvalues of matrix Λ are respectively $\lambda_1 = \frac{1}{2}(\sqrt{n-2}+\sqrt{n-4})^2 \geqslant 1$ and $\lambda_2 = \frac{1}{2}(\sqrt{n-2}-\sqrt{n-4})^2 \leqslant 1$.

Case $n = 4$: If $n = 4$, we obtain rectangular rooms, for which the number of image sources increases linearly with the layer order. Indeed, in this case, the matrix is upper triangular:

$$\Lambda = \begin{pmatrix} 1 & 2 \\ 0 & 1 \end{pmatrix}$$

with $\lambda_1 = \lambda_2 = 1$, and the computation of eq. (11) is straightforward:

$$\Lambda^i = \begin{pmatrix} 1 & 2i \\ 0 & 1 \end{pmatrix}$$

As expected, we obtain for rectangular rooms $e_i = 4(2i+1)$ and $v_i = 4$: the number of corners remains constant and equal to 4, with a linear increase of the number of edge images. And the total number of image sources $\mathfrak{N}_i$ of layer i is $\mathfrak{N}_i = e_i + v_i = 8(i+1)$, that is, increases linearly with i.

Case $n > 4$: If $n \geqslant 5$, then $\lambda_1 > 1$ and $\lambda_2 < 1$, and the eigenvectors are given by:

$$X_1 = \begin{pmatrix} \sqrt{n-2} \\ \sqrt{n-4} \end{pmatrix},\ X_2 = \begin{pmatrix} \sqrt{n-2} \\ -\sqrt{n-4} \end{pmatrix}$$

that is, Λ can be factorized into $\Lambda = S^{-1}DS$ with:

$$S = \begin{pmatrix} \frac{1}{2\sqrt{n-2}} & \frac{1}{2\sqrt{n-4}} \\ \frac{1}{2\sqrt{n-2}} & -\frac{1}{2\sqrt{n-4}} \end{pmatrix}$$

,

$$D = \begin{pmatrix} \frac{1}{2}(\sqrt{n-2}+\sqrt{n-4})^2 & 0 \\ 0 & \frac{1}{2}(\sqrt{n-2}-\sqrt{n-4})^2 \end{pmatrix}$$

and therefore:

$$S^{-1} = \begin{pmatrix} \sqrt{n-2} & \sqrt{n-2} \\ \sqrt{n-4} & -\sqrt{n-4} \end{pmatrix}$$

For large values of the layer number i, $\lambda_2^i \longrightarrow 0$, and eq. (11) reduces to:

$$\begin{pmatrix} e_i \\ v_i \end{pmatrix} \approx \frac{(\sqrt{n-2}+\sqrt{n-4})^{2i}}{2^{i+1}} \begin{pmatrix} 1 & \frac{\sqrt{n-2}}{\sqrt{n-4}} \\ \frac{\sqrt{n-4}}{\sqrt{n-2}} & 1 \end{pmatrix} \begin{pmatrix} e_0 \\ v_0 \end{pmatrix}$$

with $e_0 = v_0 = n$, that is:

$$e_i \approx \frac{n(\sqrt{n-2}+\sqrt{n-4})^{2i+1}}{2^{i+1}\sqrt{n-4}}$$
$$v_i \approx \frac{n(\sqrt{n-2}+\sqrt{n-4})^{2i+1}}{2^{i+1}\sqrt{n-2}}$$

and the total number of image sources $\mathfrak{N}_i$ of layer i is given by the sum of the two contributions, that is:

$$\begin{aligned} \mathfrak{N}_i = e_i + v_i &\approx \frac{n(\sqrt{n-2}+\sqrt{n-4})^{2i+1}}{2^{i+1}} \left(\frac{1}{\sqrt{n-4}} + \frac{1}{\sqrt{n-2}} \right) \\ &= \frac{n(\sqrt{n-2}+\sqrt{n-4})^{2(i+1)}}{2^{i+1}\sqrt{(n-2)(n-4)}} \end{aligned} \tag{12}$$

Example: For a **pentagon**, $n = 5$ and the eigenvalues are $\lambda_1 = \frac{1}{2}(\sqrt{3}+1)^2 \approx 3.73$ and $\lambda_2 = \frac{1}{2}(\sqrt{3}-1)^2 \approx 0.27$. Matrix Λ is now equal to:

$$\Lambda = \begin{pmatrix} 2 & 3 \\ 1 & 2 \end{pmatrix}$$

which reduces to:

$$\Lambda = \frac{1}{2} \begin{pmatrix} \sqrt{3} & \sqrt{3} \\ 1 & -1 \end{pmatrix} \begin{pmatrix} 2+\sqrt{3} & 0 \\ 0 & 2-\sqrt{3} \end{pmatrix} \begin{pmatrix} \frac{1}{\sqrt{3}} & 1 \\ \frac{1}{\sqrt{3}} & -1 \end{pmatrix}$$

and the total number of image sources $\mathfrak{N}_i$ of layer i is given by eq. (12):

$$\mathfrak{N}_i = e_i + v_i \approx \frac{5\left(\sqrt{3}+1\right)^{2(i+1)}}{2^{i+1}\sqrt{3}}$$

In other words, the number of image sources increases exponentially with the order of the layer, a very different behaviour than for rectangular rooms, but similar to mixing rooms [Pol92].

3.2 Convex polyhedral rooms

For convex polyhedral rooms, it is not sufficient to only consider the number N of faces. We must also consider the number n_i of edges of each face i. We thus obtain:

- the number of faces: $F = \sum_i 1 = N$
- the number of edges: since one edge is common to 2 faces, this number is $E = \frac{1}{2} \sum_i n_i$
- the number of vertices: with the assumption that vertices are shared by 3 faces only, this number is $V = \frac{1}{3} \sum_i n_i$

With the help of Euler's polyhedron formula $F - E + V = 2$, valid for convex polyhedra, we obtain:

$$F - E + V = \sum_i \left[1 - \frac{n_i}{2} + \frac{n_i}{3}\right] = \sum_i \left[1 - \frac{n_i}{6}\right] = 2$$

that is, introducing the mean number of edges per face $\bar{n} = \frac{1}{N} \sum_i n_i$:

$$(6 - \bar{n})N = 12$$

As a consequence, the mean number of edges per face, the total number of edges, and the total number of vertices are given by:

$$\bar{n} = \frac{6(N-2)}{N},\ E = 3(N-2),\ V = 2(N-2) \tag{13}$$

Note that the assumption that vertices are shared by 3 faces only does not introduce any restriction, as it is easy to "regularize" vertices shared by $m > 3$ faces by cutting-off the vertex according to Fig. 8, thus increasing by 1 the number of faces, by m the number of edges edges, and by $m - 1$ the number of vertices, that is, keeping the Euler characteristic $F - E + V$ equal to 2.

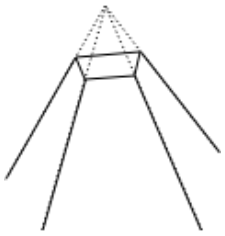

Figure 8: Regularizing vertex shared by 4 faces, by cutting-off the tip of the pyramid, thus removing one vertex but introducing 4 new edges and vertices.

As in Sect. 3.1, we consider successive layers of image rooms built around the original rooms, and we compute separately the number of free faces, edges and vertices belonging to the images created by free faces, edges an vertices. Simple enumeration leads to:

- each free face i creates:

- $N - (n_i + 1)$ free faces,
- $E - 2n_i - \sum_j \epsilon_{ij}(n_j - 3)$ free edges,
- $V - 2n_i - \sum_j \epsilon_{ij}(n_j - 4)$ free vertices,

where $\epsilon_{ij} = 1$ if faces i and j share one edge, 0 otherwise, so that $\sum_i \epsilon_{ij} = n_j$;

- each free edge k creates:
  - $N - 4$ free faces,
  - $E - 5 - \sum_j \gamma_{kj}(n_j - 3) - \sum_{lj} \delta_{klj}(n_j - 2)$ free edges,
  - $V - 6 - \sum_j \gamma_{kj}(n_j - 4) - \sum_{lj} \delta_{klj}(n_j - 3)$ free vertices,

  where $\gamma_{kj} = 1$ if edge k belongs to face j and 0 otherwise, with $\sum_j \gamma_{kj} = 2$; and where $\delta_{klj} = 1$ if edge k belongs to face j and vertex l to edge k, 0 otherwise, with $\sum_{lj} \delta_{klj} = 2$;
- each free vertex l creates:
  - $N - 3$ free faces,
  - $E - 3 - \sum_j \alpha_{lj}(n_j - 2)$ free edges,
  - $V - 4 - \sum_j \alpha_{lj}(n_j - 3)$ free vertices,

  where $\alpha_{lj} = 1$ if vertex l belongs to face j, 0 otherwise, so that $\sum_j \alpha_{lj} = 3$.

Let's now call f_m, e_m and v_m the numbers of free faces, edges and vertices respectively in layer m. We obtain the recurrence formulae:

$$
\begin{aligned}
f_{m+1} =& \sum_{i=1}^{f_m} [N - (n_i + 1)] + \sum_{k=1}^{e_m} [N - 4] + \sum_{l=1}^{v_m} [N - 3] \\
e_{m+1} =& \sum_{i=1}^{f_m} \left[E - 2n_i - \sum_j \epsilon_{ij}(n_j - 3) \right] \\
&+ \sum_{k=1}^{e_m} \left[E - 5 - \sum_j \gamma_{kj}(n_j - 3) - \sum_{lj} \delta_{klj}(n_j - 2) \right] \\
&+ \sum_{l=1}^{v_m} \left[E - 3 - \sum_j \alpha_{lj}(n_j - 2) \right] \\
v_{m+1} =& \sum_{i=1}^{f_m} \left[V - 2n_i - \sum_j \epsilon_{ij}(n_j - 4) \right] \\
&+ \sum_{k=1}^{e_m} \left[V - 6 - \sum_j \gamma_{kj}(n_j - 4) - \sum_{lj} \delta_{klj}(n_j - 3) \right] \\
&+ \sum_{l=1}^{v_m} \left[V - 4 - \sum_j \alpha_{lj}(n_j - 3) \right]
\end{aligned}
$$

Assuming that the number of image rooms increases exponentially with the layer order m, it is legitimate to replace numbers n_i and n_j by their mean $\bar{n}$, leading to the approximation:

$$\begin{aligned}
f_{m+1} \approx & f_m\,[N-\bar{n}-1] + e_m\,[N-4] + v_m\,[N-3] \\
e_{m+1} \approx & f_m\left[E-2\bar{n}-\bar{n}^2+3\bar{n})\right] + e_m\,[E-5-2(\bar{n}-3)-2(\bar{n}-2)] \\
& + v_m\,[E-3-3(\bar{n}-2)] \\
v_{m+1} \approx & f_m\left[V-2\bar{n}-\bar{n}^2+4\bar{n})\right] + e_m\,[V-6-2(\bar{n}-4)-2(\bar{n}-3)] \\
& + v_m\,[V-4-3(\bar{n}-3)]
\end{aligned}$$

that is, to the recurrence formula:

$$\begin{aligned}
\begin{pmatrix} f_{m+1} \\ e_{m+1} \\ v_{m+1} \end{pmatrix} &= \begin{pmatrix} N-\bar{n}-1 & N-4 & N-3 \\ \left(\frac{N}{2}+1\right)\bar{n}-\bar{n}^2 & \left(\frac{N}{2}-4\right)\bar{n}+5 & \left(\frac{N}{2}-3\right)\bar{n}+3 \\ \left(\frac{N}{3}+2\right)\bar{n}-\bar{n}^2 & \left(\frac{N}{3}-4\right)\bar{n}+8 & \left(\frac{N}{3}-3\right)\bar{n}+5 \end{pmatrix} \begin{pmatrix} f_m \\ e_m \\ v_m \end{pmatrix} \\
&= \Lambda^{m+1} \begin{pmatrix} f_0 \\ e_0 \\ v_0 \end{pmatrix}
\end{aligned} \tag{14}$$

with matrix Λ given by:

$$\Lambda = \begin{pmatrix} N-\bar{n}-1 & N-4 & N-3 \\ \left(\frac{N}{2}+1\right)\bar{n}-\bar{n}^2 & \left(\frac{N}{2}-4\right)\bar{n}+5 & \left(\frac{N}{2}-3\right)\bar{n}+3 \\ \left(\frac{N}{3}+2\right)\bar{n}-\bar{n}^2 & \left(\frac{N}{3}-4\right)\bar{n}+8 & \left(\frac{N}{3}-3\right)\bar{n}+5 \end{pmatrix}$$

A lengthy computation leads to the following characteristic equation for eigenvalues λ:

$$\begin{aligned}
-\lambda^3 + \lambda^2\left[\left(\frac{5N}{6}-8\right)\bar{n}+(N-9)\right] - \lambda\left[\frac{4N}{3}\bar{n}^2 - \left(\frac{26N}{3}-8\right)\bar{n}+(10N-9)\right] \\
+\left[-\frac{N}{6}\bar{n}^2+(N-1)\right] = 0
\end{aligned}$$

which, when replacing $\bar{n}$ by its value given in eq. (13), simply reduces to:

$$-\lambda^3 + \lambda^2\left[6N-49+\frac{96}{N}\right] - \lambda\left[6N-49+\frac{96}{N}\right] + 1 = 0$$

or more simply to:

$$-\lambda^3 + \lambda^2\left[\frac{6(N-4)^2}{N}-1\right] - \lambda\left[\frac{6(N-4)^2}{N}-1\right] + 1 = 0 \tag{15}$$

Case $N = 6$: If $N = 6$, we obtain rectangular parallelepiped rooms, for which eq. (13) reduces to $n_i = \bar{n} = 4$ for all i, $e_0 = 12$, and $v_0 = 8$ with $f_0 = N = 6$. In this case, the matrix is upper triangular:

$$\Lambda = \begin{pmatrix} 1 & 2 & 3 \\ 0 & 1 & 3 \\ 0 & 0 & 1 \end{pmatrix}$$

Since all diagonal terms are equal to 1, the three eigenvalues are equal to 1 and the computation of eq. (14) is straightforward:

$$\Lambda^i = \begin{pmatrix} 1 & 2i & 3i^2 \\ 0 & 1 & 3i \\ 0 & 0 & 1 \end{pmatrix}$$

We obtain for rectangular parallelepiped rooms $f_i = 6(2i+1)^2$, $e_i = 12(2i+1)$ and $v_i = 8$: as expected, the number of corners remains constant and equal to 8, with a linear increase of the number of edge images and a quadratic increase of the number of the face images. And the total number of image sources $\mathfrak{N}_i$ of layer i is $\mathfrak{N}_i = f_i + e_i + v_i = 24(i+1)^2 + 2$, that is, increases quadratically with i.

Case $N > 6$: The direct solution of eq. (15) gives then the three eigenvalues:

- $\lambda_0 = 1$,
- $\lambda_1 = \left[\frac{3(N-4)^2}{N} - 1\right] + \frac{N-4}{N}\sqrt{3[(N-6)(3N-8)]} > 1$,
- $\lambda_2 = \left[\frac{3(N-4)^2}{N} - 1\right] - \frac{N-4}{N}\sqrt{3[(N-6)(3N-8)]} < 1$.

and matrix Λ reduces to:

$$\Lambda = \begin{pmatrix} \frac{(N-2)(N-6)}{N} + 1 & N-4 & N-3 \\ \frac{3(N-2)(N-4)(N-6)}{N^2} & \frac{3(N-4)^2}{N} - 1 & \frac{3(N-3)(N-4)}{N} \\ \frac{2(N-2)(N-6)^2}{N^2} & \frac{2(N-4)(N-6)}{N} & \frac{2(N-3)(N-6)}{N} + 1 \end{pmatrix}$$

A simple matrix manipulation (see Appendix) easily gives the 3 eigenvectors associated to the 3 eigenvalues:

$$X_0 = \begin{pmatrix} (N-3) \\ 0 \\ -\frac{(N-2)(N-6)}{N} \end{pmatrix},\ X_1 = \begin{pmatrix} \sqrt{3[(N-6)(3N-8)]} \\ +\frac{3(N-6)(3N-8)}{N} \\ \frac{2(N-6)}{N}\sqrt{3[(N-6)(3N-8)]} \end{pmatrix},$$

$$X_2 = \begin{pmatrix} \sqrt{3[(N-6)(3N-8)]} \\ -\frac{3(N-6)(3N-8)}{N} \\ \frac{2(N-6)}{N}\sqrt{3[(N-6)(3N-8)]} \end{pmatrix}$$

Thus, matrix Λ can be factorized into $\Lambda = S^{-1}DS$, with the column of matrix S^{-1} equal to the eigenvectors:

$$S^{-1} = \begin{pmatrix} (N-3) & \sqrt{3[(N-6)(3N-8)]} & \sqrt{3[(N-6)(3N-8)]} \\ 0 & \frac{3(N-6)(3N-8)}{N} & -\frac{3(N-6)(3N-8)}{N} \\ -\frac{(N-2)(N-6)}{N} & \frac{2(N-6)}{N}\sqrt{3[(N-6)(3N-8)]} & \frac{2(N-6)}{N}\sqrt{3[(N-6)(3N-8)]} \end{pmatrix}$$

and matrix D given by the eigenvalues:

$$D = \begin{pmatrix} 1 & 0 & 0 \\ 0 & \frac{1}{2}\left[\sqrt{\frac{3}{N}}(N-4) + \sqrt{\frac{(N-6)(3N-8)}{N}}\right]^2 & 0 \\ 0 & 0 & \frac{1}{2}\left[\sqrt{\frac{3}{N}}(N-4) - \sqrt{\frac{(N-6)(3N-8)}{N}}\right]^2 \end{pmatrix}$$

where we have used an alternative form for the eigenvalues λ_1 and λ_2, leading by inversion to matrix S:

$$S = \frac{1}{2}\begin{pmatrix} \frac{4}{3N-8} & 0 & -\frac{2N}{(N-6)(3N-8)} \\ \frac{N-2}{(3N-8)\sqrt{3[(N-6)(3N-8)]}} & \frac{N}{3(N-6)(3N-8)} & \frac{N(N-3)}{(N-6)(3N-8)} \\ \frac{N-2}{(3N-8)\sqrt{3[(N-6)(3N-8)]}} & -\frac{N}{3(N-6)(3N-8)} & \frac{N(N-3)}{(N-6)(3N-8)} \end{pmatrix}$$

.

For large values of the layer number i, $\lambda_2^i \longrightarrow 0$, and eq. (14) is approximated by:

$$\begin{pmatrix} f_i \\ e_i \\ v_i \end{pmatrix} \approx \frac{\left[\sqrt{\frac{3}{N}}(N-4) + \sqrt{\frac{(N-6)(3N-8)}{N}}\right]^{2i}}{2^{i+1}(3N-8)}$$

$$\begin{pmatrix} N-2 & \frac{N\sqrt{3[(N-6)(3N-8)]}}{3(N-6)} & \frac{N(N-3)\sqrt{3[(N-6)(3N-8)]}}{3(N-6)} \\ \frac{(N-2)\sqrt{3[(N-6)(3N-8)]}}{N} & 3N-8 & (N-3)(3N-8) \\ \frac{3(N-2)(N-6)}{N} & 2\sqrt{3[(N-6)(3N-8)]} & 2(N-3)\sqrt{3[(N-6)(3N-8)]} \end{pmatrix}$$

$$\begin{pmatrix} f_0 \\ e_0 \\ v_0 \end{pmatrix} \tag{16}$$

Example: For a **dodecahedron**, $N = 12$ with $\bar{n} = 5$, $e_0 = 30$, and $v_0 = 20$ with $f_0 = N = 12$. The eigenvalues are $\lambda_0 = 1$, $\lambda_1 = 15 + 4\sqrt{14} \approx 29.97$ and $\lambda_2 = 15 - 4\sqrt{14} = 0.03$. Matrix Λ is now equal to:

$$\Lambda = \begin{pmatrix} 9 & 8 & 9 \\ 10 & 15 & 18 \\ 5 & 8 & 10 \end{pmatrix}$$

which reduces to:

$$\Lambda = \frac{1}{2}\begin{pmatrix} 9 & 6\sqrt{14} & 6\sqrt{14} \\ 0 & 28 & -28 \\ -5 & 6\sqrt{14} & 6\sqrt{14} \end{pmatrix}\begin{pmatrix} 1 & 0 & 0 \\ 0 & 15+4\sqrt{14} & 0 \\ 0 & 0 & 15-4\sqrt{14} \end{pmatrix}$$

$$\begin{pmatrix} \frac{1}{7} & 0 & -\frac{1}{7} \\ \frac{5}{84\sqrt{14}} & \frac{1}{84} & \frac{9}{28} \\ \frac{5}{84\sqrt{14}} & -\frac{1}{84} & \frac{9}{28} \end{pmatrix}$$

and the total number of image sources $\mathfrak{N}_i$ of layer i is given by the sum of the 3 terms in eq. (16), that is:

$$\mathfrak{N}_i = f_i + e_i + v_i \approx \frac{\left(15+4\sqrt{14}\right)^i}{46}\Big(5\left[4+\sqrt{14}\right]f_0 + 2\left[15+2\sqrt{14}\right]e_0 + 37\left[7+4\sqrt{14}\right]v_0\Big) = \frac{10(29.97)^i\left(316+157\sqrt{14}\right)}{23}$$

In other words, the number of image sources increases exponentially with the order of the layer, as is the case for polygonal rooms with more than 4 edges.

Note that the case of vertices shared by more than 3 faces is obtained by first regularising them according to Fig. 8, then moving the intersecting face toward the original vertex: the number of image rooms remains constant. Therefore, assuming that all vertices are shared by 3 faces only does not introduce any restriction.

3.3 Case of reflex angles

The case of reflex angles can now be handled by noticing that reflex angles do not introduce new images. For polygons, the two adjacent edges must be considered as a unique edge, thus diminishing the number of edges and vertices by one. For polyhedra, the two adjacent faces becomes one unique face, thus diminishing the number of faces and edges by one. However, when two reflex dihedral angles share a common vertex between two common adjacent edges, the two adjacent edges also coalesce into one single edge, diminishing both the number of edges and the number of vertices by one, thus keeping Euler characteristic constant and equal to 2.

3.4 Case of acute angles

The case of acute angles can also be handled by noticing that they introduce several new images, depending on the angle. However, both for polygons and for polyhedra, each case must be handled specifically.

4 Visible image sources

In the previous section, we have demonstrated that, except for rectangular rooms, the number of image sources increases exponentially, most of them creating diffracted rays, due to the excess angles at the hinges (see Sec. 2). They correspond to what is usually called "hidden image sources", that is, image sources that are not visible from the receiver. We therefore now address the question of the visible images, and the related question of their *horizon of visibility*, which we define as the distance at which visible image sources smear within the swarm of image sources because the intensity they radiate into the original room starts decreasing exponentially with distance. In doing so, we must handle separately the cases of regular polygons and polyhedra, and the case of irregular ones.

4.1 Regular polygons and polyhedra

The most striking feature of space tessellation by regular polygons or polyhedra (Fig. 9) is the fact that any grouping of one cell and its image on any of its edges or faces displays parallel edges or faces. As a consequence, images sources are visible at long range along some specific discrete directions. Nevertheless, every now and then, one image source becomes hidden behind some hinge, even in these specific directions (red rays in Fig. 9), so that one should rather talk of *channels* - in green in Fig. 9.

It can be seen in Fig. 9 that channels are defined by the repetition of patterns along some discrete directions. The number of these directions is numerable, since there is a numerable number of image sources; and the widths of

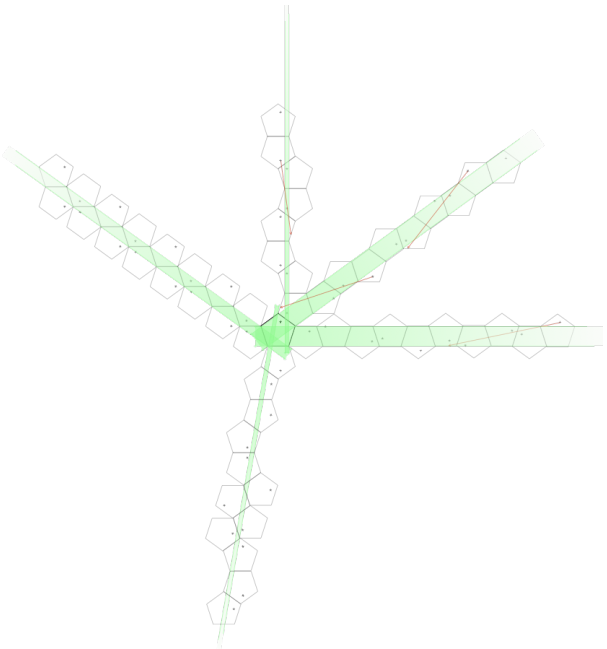

Figure 9: Visible (green rays) and invisible (red rays) images for a regular pentagon. Notice the long-range visibility in some direction.

the channels decrease with the length of the repetition pattern. In any case, at some distance, the widths of the channels become narrow enough so that path differences for all rays joining the image sources to the original room must be taken into account, as they eventually reduce the intensity of the sources when they become narrower that the first Fresnel zones around the direct rays. As a consequence, all distant visible sources eventually radiate an exponentially decreasing intensity, no longer inversely proportional to the square of the travelled distance. In that respect, distant sources do not differ from hidden sources; but the distances at which these transitions operate are frequency dependant, increasing with frequency.

The number of visible images at any range increases at most with distance in the polygon case, and squared distance in the polyhedra case. This is a consequence of Fig. 9, since the cells corresponding to visible images constitute a subset of the Euclidean plane in which the original room lays, bordered by bold lines in the Figure. As the average number of cells in any annulus, resp. any shell, of inner and outer radii d and $d + \Delta d$ is overestimated by dividing its surface by the surface S of the cell, resp. its volume by the volume V of the cell, an overestimation for the number of visible images at distance d is therefore $\frac{2\pi d \Delta d}{S}$, resp. $\frac{4\pi d^2 \Delta d}{V}$, which increases at most with the distance for a polygon, and with the squared distance for a polyhedron. Thus, the number of hidden sources will quickly outnumber the number of visible sources, thus diluting their strength.

Can we evaluate the *horizon for visible sources*? From the above discussion and definition, the maximum distance of visibility can be estimated from the width w of the channel and the wavelength λ of the frequency under consider-

ation as a few times the distance H defined by:

$$H \approx \frac{w^2}{\lambda} \tag{17}$$

Note that no horizon exists for rectangular rooms as no scattering occurs on the vertices, resp. the edges, since no excess angle exists at vertices or edges through reflections.

4.2 Irregular polygons and polyhedra

Space tessellation by irregular polygons or polyhedra (Fig. 10) does not exhibit parallel edges or faces after reflections, and no specific patterns are repeated along any direction. Indeed, as can be seen in Fig. 10, all channels eventually split in narrower ones as they cross some hinges, a process which is signalled by blue arrows in Fig. 10. As a consequence, the horizon of visibility of the image sources is much shorter than in the regular case.

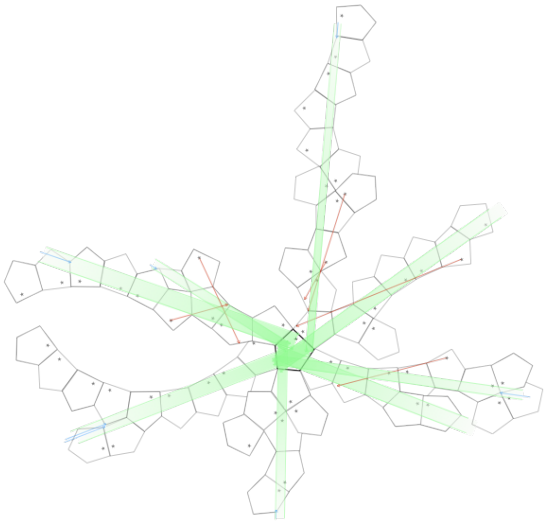

Figure 10: Visible (green rays) and invisible (red rays) images for an irregular pentagon. Blue arrows signal channel splitting at hinges. Notice that visibility quickly vanishes due to random distribution of hinges (here, all vertices).

As can be seen in Fig. 10, the orientations of the image rooms gradually become random with distance, as the angles between non-adjacent, opposing edges or faces are no longer rational ratios of 2π. This creates random distribution of the hinges, and thus the splitting of the channels and eventually scattering. As a consequence, the horizon of visibility of the image sources can be estimated as a few times the characteristic sizes of the cells, at most 10 times in Fig. 10.

5 Taking scattering in account: conservation of stress-energy tensor

Up to now, we have not considered the nature of the signals emitted by the sources. As we are interested in sound waves, the wave properties of the field has to be taken into account. Thus, a time dimension must be added to the space of Sec. 2.1 in order to introduce the wave equation.

5.1 Wave equation and stress-energy tensor

From now on, we consider a 4-dimensional time-space with its metric tensor g_{ij} and the volume element $dV = \sqrt{|g|}dx^0 \dots dx^3$, where $g = \det g_{ij}$ [Lin 5]. But now, g is *negative* as the first eigenvalue of the metric tensor is negative and equal to $-c^2$, where c is the speed of sound: its eigenvector corresponds to the time direction dx^0. The infinitesimal distance element is still given by eq. 1:

$$ds^2 = g_{ij}dx^i dx^j \tag{18}$$

Therefore, covariant derivation, Christoffel symbols, Riemann and Ricci tensor as well as the scalar curvature are still defined as in Sec. 2.1. More precisely, according to Sec. 2.3, we have:

$$g_{ij} = \begin{pmatrix} -c^2 & 0 & 0 & 0 \\ 0 & 1 & \mathrm{sgn}(x^1)\mathrm{sgn}(x^2)\cos\beta & 0 \\ 0 & \mathrm{sgn}(x^1)\mathrm{sgn}(x^2)\cos\beta & 1 & 0 \\ 0 & 0 & 0 & 1 \end{pmatrix} \tag{19}$$

$$g^{ij} = \begin{pmatrix} -c^{-2} & 0 & 0 & 0 \\ 0 & \frac{1}{\sin^2\beta} & -\frac{\mathrm{sgn}(x^1)\mathrm{sgn}(x^2)\cos\beta}{\sin^2\beta} & 0 \\ 0 & -\frac{\mathrm{sgn}(x^1)\mathrm{sgn}(x^2)\cos\beta}{\sin^2\beta} & \frac{1}{\sin^2\beta} & 0 \\ 0 & 0 & 0 & 1 \end{pmatrix}$$

where β is one fourth of the total dihedral angle around the hinge, and with determinant $g = -c^2 \sin^2\beta < 0$. g_{ij} and g^{ij} reduce to diagonal matrices on the arms, now denoted ($x^1 = 0$ and $x^2 = 0$), with all diagonal elements equal to 1 except $g_{00} = -c^2$ and $g^{00} = -c^{-2}$, and with $g = -c^2$. As for the Christoffel symbols, they are all equal to 0, but for $\Gamma^2_{11} = 2\delta(x^1)\mathrm{sgn}(x^2)\cos\beta$ and $\Gamma^1_{22} = 2\mathrm{sgn}(x^1)\delta(x^2)\cos\beta$ (eq 7); and all elements of the Ricci tensor are 0 except $R_{11} = R_{22} = 4\delta(x^1)\delta(x^2)\cos\beta < 0$ (eq. 8). The scalar curvature therefore remains $R = 8\delta(x^1)\delta(x^2)\cos\beta < 0$, but the local curvature, obtained by integrating half the scalar curvature over a small space element, is now equal to $\frac{1}{2}\int R\sqrt{|g|}dx^0dx^1dx^2dx^3$. It remains null everywhere - flat space - except on the hinges, now given by the apical edges extended by the time laps. In the limit where β tends toward a right angle, the curvature around any hinge is equal to $c(2\pi - 4\beta)\ell\Delta t < 0$, where ℓ is the length of the corresponding apical edge and Δt the time lag.

We now introduce the wave equation:

$$\Box\Phi = \nabla_i g^{ij}\partial_j\Phi = 0 \tag{20}$$

where Φ is the velocity potential. Pressure p and particle velocity v are obtained from the velocity potential as covectors:

$$p = \rho \partial_0 \Phi$$

$$v_i = -\partial_i \Phi$$

where i takes value 1, 2 or 3 (space variables), and where ρ is the density of the fluid in which the waves propagate. Note that it is more useful to use the vector formulations for these two quantities:

$$v^i = -\nabla^i \Phi = -g^{ij} \partial_j \Phi \tag{21}$$

meaning that:

$$v^0 = -\nabla^0 \Phi = -g^{00} \partial_0 \Phi = c^{-2} \partial_0 \Phi = \frac{p}{\rho c^2}$$

In general, the velocity potential Φ is a complex function. We therefore consider the product $\partial_k \Phi^* \Box \Phi$. Differentiation rules lead to:

$$\begin{aligned} \partial_k \Phi^* \Box \Phi = \partial_k \Phi^* \nabla_i g^{ij} \partial_j \Phi &= \nabla_i g^{ij} \left[\partial_k \Phi^* \partial_j \Phi \right] - \left[\nabla_i \partial_k \Phi^* \right] g^{ij} \partial_j \Phi \\ &= \nabla_i g^{ij} \left[\partial_k \Phi^* \partial_j \Phi \right] - \left[\nabla_k \partial_i \Phi^* \right] g^{ij} \partial_j \Phi \\ &= \nabla^j \left[\partial_k \Phi^* \partial_j \Phi \right] - \left[\nabla_k \partial_i \Phi^* \right] g^{ij} \partial_j \Phi = 0 \end{aligned}$$

As i and j are mute indices, keeping only the real part of the preceding equation leads to:

$$\nabla^j \left(\partial_j \Phi^* \partial_k \Phi + \partial_j \Phi \partial_k \Phi^* \right) = \nabla_k \left(\partial_i \Phi^* g^{ij} \partial_j \Phi \right) \tag{22}$$

that is, to:

$$\nabla^i T_{ij} = 0 \tag{23}$$

where T_{ij} is the *symmetrical* stress-energy tensor, defined by:

$$T_{ij} = \frac{\partial_i \Phi^* \partial_j \Phi + \partial_i \Phi \partial_j \Phi^*}{2} - \frac{1}{2} g_{ij} \left(\partial_i \Phi^* g^{ij} \partial_j \Phi \right) \tag{24}$$

It is easy to recognise that the eq. (23) corresponds to the contravariant conservation of the stress-energy tensor.

5.2 Conservation of stress-energy tensor

The conservation of the stress-energy tensor takes a simpler form for T^{ij} than for T_{ij}, which still is symmetric. Indeed, Eq (23) can be written as:

$$g^{lj} \nabla^i T_{il} = g^{ik} \nabla_k T_{il} g^{lj} = \nabla_i T^{ij} = \partial_i T^{ij} + \Gamma^i_{ik} T^{kj} + \Gamma^j_{ik} T^{ik} = 0$$

that is ([Lin 5] p.54):

$$\frac{1}{\sqrt{|g|}} \partial_i (\sqrt{|g|} T^{ij}) + \Gamma^j_{ik} T^{ik} = 0$$

or, after integration on a small 4-dimensional volume V with border ∂V:

$$\int_{\partial V} n_i T^{ij} dS + \int_V \Gamma^j_{ik} T^{ik} dV = 0 \tag{25}$$

In the last equation, n_i is the outgoing normal covector to the boundary, normalized by $n_i g^{ij} n_j = \pm 1$, with a negative sign for time boundaries. If part of the border ∂V is defined by equation $f(x^0 \dots x^3) = 0$, then n_i is given by:

$$n_i = \frac{\pm \partial_i f}{\sqrt{\pm \partial_i f g^{ij} \partial_i f}}$$

where the same sign is used in the numerator and the denominator. And dS is the volume element of the border induced by the metric on ∂V. In other words, it includes the term $\sqrt{|g|}$.

In eq. (25), $T^{ij} = \frac{1}{2}\left[g^{ik}(\Phi_k \Phi_l^* + \Phi_k^* \Phi_l) g^{lj} - g^{ij}\left(\partial_i \Phi^* g^{ij} \partial_j \Phi\right)\right]$ can also be written:

$$T^{ij} = \frac{1}{2}\left[(\Phi^i \Phi^{j*} + \Phi^{i*} \Phi^j) - g^{ij}\left(\Phi^{i*} g_{ij} \Phi^j\right)\right]$$

where the Φ_i, resp. the Φ^j, are the partial covariant derivatives, resp. partial contravariant derivatives, of the velocity potential Φ. Note that the last form is preferred, as it makes use of vectors instead of covectors.

$\left(\Phi^{i*} g_{ij} \Phi^j\right)$ is then given by:

$$\begin{aligned}\left(\Phi^{i*} g_{ij} \Phi^j\right) = \big[&-c^2|\Phi^0|^2 + |\Phi^1|^2 + |\Phi^2|^2 + |\Phi^3|^2 \\ &+ 2\mathrm{sgn}(x^1)\mathrm{sgn}(x^2)\cos\beta \Re(\Phi^1 \Phi^{2*})\big]\end{aligned}$$

and T^{ij} by:

$$\begin{pmatrix}
\frac{c^{-2}}{2}\left[c^2|\Phi^0|^2 + |\Phi^1|^2 + |\Phi^2|^2 + |\Phi^3|^2 + 2\mathrm{sgn}(x^1)\mathrm{sgn}(x^2)\cos\beta\Re(\Phi^1\Phi^{2*})\right] & \Re(\Phi^0\Phi^{1*}) & \Re(\Phi^0\Phi^{2*}) & \Re(\Phi^0\Phi^{3*}) \\
\Re(\Phi^0\Phi^{1*}) & \frac{\sin^{-2}\beta}{2}\left[c^2|\Phi^0|^2 - \cos 2\beta|\Phi^1|^2 - |\Phi^2|^2 - |\Phi^3|^2 - 2\mathrm{sgn}(x^1)\mathrm{sgn}(x^2)\cos\beta\Re(\Phi^1\Phi^{2*})\right] & \frac{\Re(\Phi^1\Phi^{2*})}{\sin^4\beta} + \frac{\mathrm{sgn}(x^1)\mathrm{sgn}(x^2)\cos\beta}{2\sin^2\beta}\left[-c^2|\Phi^0|^2 + |\Phi^1|^2 + |\Phi^2|^2 + |\Phi^3|^2\right] & \Re(\Phi^1\Phi^{3*}) \\
\Re(\Phi^0\Phi^{2*}) & \frac{\Re(\Phi^1\Phi^{2*})}{\sin^4\beta} + \frac{\mathrm{sgn}(x^1)\mathrm{sgn}(x^2)\cos\beta}{2\sin^2\beta}\left[-c^2|\Phi^0|^2 + |\Phi^1|^2 + |\Phi^2|^2 + |\Phi^3|^2\right] & \frac{\sin^{-2}\beta}{2}\left[c^2|\Phi^0|^2 - |\Phi^1|^2 - \cos 2\beta|\Phi^2|^2 - |\Phi^3|^2 - 2\mathrm{sgn}(x^1)\mathrm{sgn}(x^2)\cos\beta\Re(\Phi^1\Phi^{2*})\right] & \Re(\Phi^2\Phi^{3*}) \\
\Re(\Phi^0\Phi^{3*}) & \Re(\Phi^1\Phi^{3*}) & \Re(\Phi^2\Phi^{3*}) & \frac{1}{2}\left[c^2|\Phi^0|^2 - |\Phi^1|^2 - |\Phi^2|^2 + |\Phi^3|^2 - 2\mathrm{sgn}(x^1)\mathrm{sgn}(x^2)\cos\beta\Re(\Phi^1\Phi^{2*})\right]
\end{pmatrix}$$

As for the conservation of the stress-energy tensor, it reduces to:

$$\begin{aligned}
&\int_{\partial V} n_i T^{i0} dS = 0 \\
&\int_{\partial V} n_i T^{i1} dS + \int_V \Gamma^1_{22} T^{22} dV = 0 \\
&\int_{\partial V} n_i T^{i2} dS + \int_V \Gamma^2_{11} T^{11} dV = 0 \\
&\int_{\partial V} n_i T^{i3} dS = 0
\end{aligned}$$

that is to:

$$\begin{aligned}
&\int_{\partial V} n_i T^{i0} dS = 0 \\
&\int_{\partial V} n_i T^{i1} dS = -2\cos\beta \int_V \mathrm{sgn}(x^1)\delta(x^2) T^{22} \sqrt{|g|} dx^0 dx^1 dx^2 dx^3 \\
&\int_{\partial V} n_i T^{i2} dS = -2\cos\beta \int_V \delta(x^1)\mathrm{sgn}(x^2) T^{11} \sqrt{|g|} dx^0 dx^1 dx^2 dx^3 \\
&\int_{\partial V} n_i T^{i3} dS = 0
\end{aligned} \tag{26}$$

Note that the expression of T^{11} and T^{22} on the arms must be used on the left hand side of eq. (26), that is:

$$\begin{aligned}
T^{11} &= \frac{1}{2}\left[c^2|\Phi^0|^2 + |\Phi^1|^2 - |\Phi^2|^2 - |\Phi^3|^2\right] \\
T^{22} &= \frac{1}{2}\left[c^2|\Phi^0|^2 - |\Phi^1|^2 + |\Phi^2|^2 - |\Phi^3|^2\right]
\end{aligned} \tag{27}$$

which are positive.

In other words, when the stress-energy tensor crosses the arm Ox^2 of the angle, it receives a positive acceleration proportional to T^{22} in the x^1 direction; and when it crosses the arm Ox^1 of the angle, it receives a positive acceleration proportional to T^{11} in the x^2 direction. However, it does not correspond to a deviation of the direction of propagation since the space is flat everywhere but on the hinge. It only takes into account the change of coordinates across the arms of the angle.

5.3 Ray scattering

Any ray issued from a sound source will have some thickness. This is simply due to the uncertainty principle (see for example [Ste10]), which states that position and direction cannot be both determined with infinite precision. Note that this is not the case with the geometrical constructions of the previous Sections, where both are simultaneously defined with infinite precision.

According to Hadamard [Had03], waves are discontinuities that move through space. These discontinuities can be infinitesimal, and they are defined by a function $f(x^0, x^1, x^2, x^3) = 0$ on the time-space variables. As a consequence, the velocity potential Φ can be expressed as a function of f, and the wave can be defined by the equation $\left(\Phi^{i*} g_{ij} \Phi^j\right) = 0$, or equivalently $\left(f^{i*} g_{ij} f^j\right) = 0$.

We now consider a wave packet, that is, a wave of finite extension, both along the direction of propagation defined by the vector $\nabla^i f$, and laterally along $f(x^i) = 0$. The uncertainty principle then states that frequency and wave numbers are defined as distribution, the standard deviations of which verify $\Delta x^i \Delta k_i \geqslant \frac{1}{2}$, with $k_0 = \omega = 2\pi f$ the radian frequency.

We then introduce new coordinates ξ^i, defined by $\xi^0 = cx^0$, $\xi^1 = f(x^i)$ (along $\nabla^i f$), ξ^2 and ξ^3 on the surfaces $f(x^i) = 0$ at time ξ^0. As distance must be independent of coordinate systems:

$$g_{ij} dx^i dx^j = \gamma_{kl} d\xi^k d\xi^l = \gamma_{kl} \frac{\partial \xi^k}{\partial x^i} \frac{\partial \xi^l}{\partial x^j} dx^i dx^j$$

that is, $g_{ij} = \gamma_{kl} \frac{\partial \xi^k}{\partial x^i} \frac{\partial \xi^l}{\partial x^j}$, where γ_{kl} is the metric tensor associated with the new coordinates ξ^i. As a consequence, $|g| = |\gamma| |\frac{\partial \xi^k}{\partial x^i}|^2$, where g, γ and $|\frac{\partial \xi^k}{\partial x^i}|$ are determinants. We can further write that $d\xi^1 = c_i dx^i$, with $c_0 = -c$ and c_i, $i = 1, 2, 3$ the direction cosines of the wave packet. The wave packet is therefore completely defined by its distribution on any hyper-surface that crosses its trajectory. On the other hand, on any hyper-surface parallel to the trajectory, the distribution will depend on the distance to the trajectory.

We now can apply the stress-energy conservation eq. (26) to our wave packet. We choose for integration a time interval over which the wave packet moves from one side of the angle arms to the other. Two cases are depicted in Fig. 11.

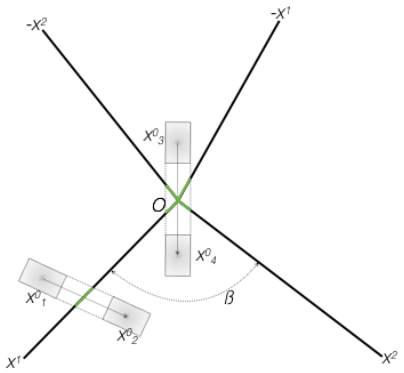

Figure 11: Wave packets crossing angle arms. Packet on the left crosses arm Ox^1 between x_1^0 and x_2^0; packet in the middle symmetrically crosses the two arms. Green lines mark the areas where deviations occur.

The first wave packet is located in sector $(-x^2)Ox^1$ at time x_1^0. It is here defined by the projection of its distribution on the plane of Fig. 11, where it is represented by a rectangle area with levels of grey proportional to the probability of presence of the wave packet. The size of the rectangle is chosen such that the components of the stress-energy tensor are negligible on its boundaries. As time increases, the wave packet moves at angle θ with respect to direction x^2 toward sector x^1Ox^2 in which it is located at time x_2^0. In the sector $(-x^2)Ox^1$,

at time x_1^0, we have therefore:

$$\left(\Phi^{i*} g_{ij} \Phi^j\right) = \left[-c^2|\Phi^0|^2 + |\Phi^1|^2 + |\Phi^2|^2 + |\Phi^3|^2 - 2\cos\beta\Re(\Phi^1\Phi^{2*})\right] = 0$$
$$T^{00} = \frac{1}{2c^2}\left[c^2|\Phi^0|^2 + |\Phi^1|^2 + |\Phi^2|^2 + |\Phi^3|^2 - 2\cos\beta\Re(\Phi^1\Phi^{2*})\right]$$
$$T^{01} = \Re(\Phi^0\Phi^{1*}),\ T^{02} = \Re(\Phi^0\Phi^{2*}),\ T^{03} = \Re(\Phi^0\Phi^{3*})$$

and these components remain constant as long as the wave packet remains in sector $(-x^2)Ox^1$. Note that the first equation, which expresses that Φ corresponds to a wave packet, can be rewritten as:

$$c^2|\Phi^0|^2 = |\Phi^1|^2 + |\Phi^2|^2 + |\Phi^3|^2 - 2\cos\beta\Re(\Phi^1\Phi^{2*}) \tag{28}$$

It crosses arm Ox^1 ($x^2 = 0$) in-between times x_1^0 and x_2^0, where it is deviated according to the second line of eq. (26). In other words, the components of T^{ij} do not change, but for component T^{01} which becomes, according to eq. (26):

$$\int_{\partial V_{x_2^0}} n_0 T^{01} dS = -2\cos\beta \int_V \mathrm{sgn}(x^1)\delta(x^2) T^{22}\sqrt{|g|}dx^0dx^1dx^2dx^3 + \int_{\partial V_{x_1^0}} n_0 T^{01} dS \tag{29}$$

where $\partial V_{x_1^0}$, resp. $\partial V_{x_2^0}$ is the boundary at time x_1^0, resp. x_2^0, that is, the volumes of the wave packet at x_1^0 and x_2^0, and the components of T^{ij} are negligible on the boundaries of the wave packet. Simple calculations then shows that $n_0 = -c$ and $dS = \sin\beta dx^1dx^2dx^3$ on $\partial V_{x_1^0}$ and $\partial V_{x_2^0}$, with $dV = c\sin\beta dx^0dx^1dx^2dx^3$ which reduces to $dV_{x^2=0} = cdx^0dx^1dx^2dx^3$ on the arm $x^2 = 0$.

Similarly, on the arm $x^2 = 0$, T^{22} is given by eq. (27), that is, with the help of eq. (28):

$$T^{22} = |\Phi^2|^2 - \cos\beta\Re(\Phi^1\Phi^{2*})$$

According to eq. (21), we have $\Phi^i = -v^i$, so that the previous equation becomes:

$$T^{22} = |v^2|^2 - \cos\beta\Re(v^1v^{2*})$$

with the v^i represented in Fig. 12, except for v^3 which is perpendicular to the plane of the figure. Also note that the figure presents the projections of cv_1^0 and cv_2^0 on the plane Ox^1x^2, respectively called v_1 and v_2.

With the help of Fig. 12, it can easily be seen that eq. (28) is equivalent to the vector equation $c\vec{v^0} = \vec{v^1} + \vec{v^2} + \vec{v^3}$, that is, by projecting on v^2:

$$c\vec{v^0}\cdot\vec{v^{2*}} = \vec{v^1}\cdot\vec{v^{2*}} + \vec{v^2}\cdot\vec{v^{2*}} + 0 = cv^0v^{2*}\cos\theta$$

with $\vec{v^1}\cdot\vec{v^{2*}} = v^1v^{2*}\cos(\pi - \beta)$. We therefore recover:

$$c\Re(\vec{v^0}\cdot\vec{v^{2*}}) = |v^2|^2 - \Re(v^1v^{2*})\cos\beta$$
$$= |\Phi^2|^2 - \cos\beta\Re(\Phi^1v^{\Phi*}) = c\cos\theta\Re(\Phi^0\Phi^{2*})$$

where $\cos\theta = c_2$ is the direction cosine of vector $\vec{v^0}$ with respect to axis Ox^2. In Fig. 12, it corresponds to the projection of c_2 on the plane Ox^1x^2. All in all, we obtain on the arm $x^2 = 0$:

$$T^{22} = c_2\Re(c\Phi^0\Phi^{2*}) \tag{30}$$

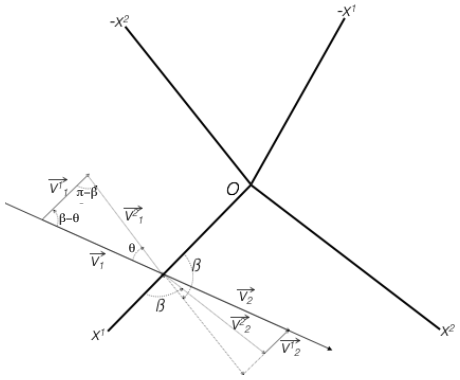

Figure 12: Wave packets travelling at angle δ with respect to arm Ox^2. v_j^i are the components of the particle velocity vector, with v_1 and v_2 the projections of cv_1^0 and cv_2^0 on the plane Ox^1x^2. Note that $\theta < 0$ since v_j^1 are negative.

We must carry out the integration $\int_V \mathrm{sgn}(x^1)\delta(x^2)T^{22}\sqrt{|g|}dx^0dx^1dx^2dx^3$ on arm Ox^2. Taking into account that $\frac{\partial\xi^1}{\partial x^2} = c_2$, we obtain $\delta(x^2) = \frac{\delta(\xi^1-\xi)}{c_2}$, where ξ is the value taken by ξ^1 on the axis Ox^2. Then using the relation between old and new coordinates x^i and ξ^i, we obtain:

$$\begin{aligned}
&\int_V \mathrm{sgn}(x^1)\delta(x^2)T^{22}\sqrt{|g|}dx^0dx^1dx^2dx^3 \\
&\qquad = \int_V \frac{\delta(\xi^1-\xi)}{c_2} c_2 \Re(c\Phi^0\Phi^{2*})\sqrt{|\gamma|}d\xi^0d\xi^1d\xi^2d\xi^3 \\
&\qquad = \int_V \Re(c\Phi^0\Phi^{2*})\sqrt{|\gamma|}d\xi^0d\xi^2d\xi^3
\end{aligned}$$

and with the help of eq. (29):

$$\begin{aligned}
-c\overline{T^{01}}_{\partial V_{x_2^0}} &= \int_{\partial V_{x_2^0}} n_0 T^{01} dS \\
&= -2\cos\beta \int_V \mathrm{sgn}(x^1)\delta(x^2)T^{22}\sqrt{|g|}dx^0dx^1dx^2dx^3 + \int_{\partial V_{x_1^0}} n_0 T^{01} dS \\
&= -2\cos\beta \int_{\partial V_{x^2=0}} \Re(c\Phi^0\Phi^{2*})\sqrt{|\gamma|}d\xi^0d\xi^2d\xi^3 - c\overline{T^{01}}_{\partial V_{x_1^0}} \\
&= -2c\cos\beta\overline{\Re(\Phi^0\Phi^{2*})}_{x^2} - c\overline{T^{01}}_{\partial V_{x_1^0}}
\end{aligned}$$

or simply:

$$\overline{T^{01}}_{\partial V_{x_2^0}} = \overline{T^{01}}_{\partial V_{x_1^0}} + 2\cos\beta\overline{\Re(\Phi^0\Phi^{2*})}_{x^2} \tag{31}$$

In other word, Φ^1 is "*augmented*" with $2\cos\beta\Phi^2$, as is visible in Fig. 12 where $\cos\beta < 0$.

This is not the case for the second wave packet, located in sector $(-x^1)O(-x^2)$ at time x_3^0 and moving to sector x^1Ox^2 at time x_4^0. It symmetrically crosses the arms $x^1 = 0$ and $x^2 = 0$ on its way. Since the function sgn changes sign around

the origin O, the negative deviation compensates for the positive one on each axis, and no deviations occurs. However, if a larger part of the packet passes on one side of the origin, some deviation occurs in proportion of the offset. This case is not represented in Fig. 11.

In both cases, direct calculation shows that T^{00} does not change when crossing arm Ox^1, as expected for energy conservation.

Note that, in the case of a wave packet impinging at near grazing incidence on a reflex angle, the above formalism recovers the sound particle diffraction model of [Ste10]. However, it takes into account the angle of the scattering wedge and the scattering of the image wave packet, both of which are absent from the sound particle diffraction model.

6 Conclusion

We have presented a geometrical theory that naturally accounts for scattering on the boundaries of a room. It introduces Riemannian spaces with negative curvature, which constitute the proper setting for the distribution of images created by non-rectangular rooms with obtuse angles, that is, created by irregular polyhedra. The crucial factor is the excess angle that arises around specific edges, called hinges, when first and second order images are considered, as it pilots the metric tensor of the space and all its geometrical properties, including its curvature. In the case of reflex and acute dihedral angles around edges, less, resp. more, reflection orders must be taken into account to properly tessellate the Riemannian space.

From this Riemannian tessellation, we have proposed a scheme for counting the number of image sources. Here, the parameter is not the order of reflection, but counting the layers of images around the original room. Only free faces, edges and vertices are taken into account to build the layers, and it makes it possible to give a close form formula for the number of image sources in case all dihedral angles are obtuse: the number of images increases exponentially, making polyhedral rooms similar to mixing rooms in this respect. We did not explicitly solved for the cases when some dihedral angles are reflex or acute, but gave some indications as how to handle them.

In the case of regular polygons and polyhedra, we have also shown that image sources are regularly distributed along channels delimited by repetitive distributions of hinges and becoming narrower when the repetitive patterns of image rooms become longer. In the case of irregularly shaped rooms, the channels split randomly since the distribution of hinges is also random. In both cases, we have defined the horizon of visibility as the distance at which the width of the channel becomes narrower than the first Fresnel zone, thus creating an exponential decrease of the image sources with distance.

Lastly, using the curvature on the hinges and complementing it with the uncertainty principle, we were able to describe the scattering of wave packets around dihedral angles. The scattering is proportional to the excess angle, and is best described in terms of the stress-energy tensor, that is, in terms of energy conservation. The basic elements for computing the scattering are given, and must be adapted to each case at hand in order to derive formulae.

The present theory must now be developed to derive scattering coefficients from the distribution of hinges around a room. Most certainly, the excess angles

are the main factors, complemented by the lengths of the hinges. But wave length also plays a rôle, as demonstrated in Sections 4 and 5.3. Proper definition of scattering coefficients has long been missing for the application of the diffusion equation in Room Acoustics [PPS97], despite some recent attempts [GD̈21].

There remain to introduce absorption in the present theory. Due to its geometrical nature, the present theory cannot account for losses in its present form. The classical way to introduce absorption, which consider intensity flows inside the boundaries, cannot be used here without some adaptation. But accounting for losses should not proove difficult since absorption is easily described with the stress-energy tensor used in the last Section, as shown in [DPTP17, DPTP18].

Appendix: factorization of matrix Λ

Remembering that Λ is given by:

$$\Lambda = \begin{pmatrix} \frac{(N-2)(N-6)}{N} + 1 & N-4 & N-3 \\ \frac{3(N-2)(N-4)(N-6)}{N^2} & \frac{3(N-4)^2}{N} - 1 & \frac{3(N-3)(N-4)}{N} \\ \frac{2(N-2)(N-6)^2}{N^2} & \frac{2(N-4)(N-6)}{N} & \frac{2(N-3)(N-6)}{N} + 1 \end{pmatrix}$$

it is easy to see that, if one subtracts the eigenvalue 1 from all its line, the first and last line become proportional with a factor $\frac{2(N-6)}{N}$. Then subtracting $\frac{3(N-4)}{N}$ time the first line from the second one, the second coordinate of the corresponding eigenvector must be null. The fist line then give a relation between the first and the last coordinates, from which the first eigenvector is derived:

$$X_0 = \begin{pmatrix} (N-3) \\ 0 \\ -\frac{(N-2)(N-6)}{N} \end{pmatrix}$$

Using the form $\left[\frac{3(N-4)^2}{N} - 1\right] \pm \frac{N-4}{N}\sqrt{3[(N-6)(3N-8)]}$ for the two other eigenvalues, they are easily subtracted from the diagonal terms of matrix Λ. Then subtracting $\frac{2(N-6)}{N}$ times the first line from the last one gives a relation between the first and the last coordinates: the last coordinates is equal to $\frac{2(N-6)}{N}$ times the first one. Introducing this relationship into the second line gives a first coordinate proportional to $\sqrt{3[(N-6)(3N-8)]}$, from which the other coordinates are obtained. In the end, the corresponding eigenvectors is given by:

$$X = \begin{pmatrix} \sqrt{3[(N-6)(3N-8)]} \\ \pm\frac{3(N-6)(3N-8)}{N} \\ \frac{2(N-6)}{N}\sqrt{3[(N-6)(3N-8)]} \end{pmatrix}$$

with sign + on the second line corresponding to λ_1 and sign $-$ to λ_2.

References

[CM78] L. Cremer and H.A. Müller. *Die wissenschaftlichen Grundlagen der Raumakustik*, volume Band I, page 25. Hirzel Verlag, 1978.

[DPTP17] H. Dujourdy, B. Pialot, T. Toulemonde, and J.D. Polack. An energetic wave equation for modelling diffuse sound fields – application to corridors. *Acta Acustica*, 103:480–491, 2017.

[DPTP18] H. Dujourdy, B. Pialot, T. Toulemonde, and J.D. Polack. An energetic wave equation for modelling diffuse sound fields – application to open offices. *Wave Motion*, 2018.

[GÜ21] Z.S. Gül. Exploration of room acoustics coupling in Hagia Sophia of Istanbul for its different states. *J. Acoust. Soc. Am.*, 149(1):320–339, January 2021.

[Had03] J. Hadamard. *Leçons sur la propagation des ondes et les équations de l'hydrodynamique*. Librairie Scientifique A. Hermann, Paris, 1903.

[Lin 5] B. Linet. Notes de cours de relativité générale, 2004-5.

[NE93] G. Naylor Ed. Special issue on computer modelling and auralisation of sound fields in rooms. *Applied Acoustics*, 38(2-4), 1993.

[Pol92] J.D. Polack. Modifying chambers to play billiards: the foundations of reverberation theory. *Acustica*, 76:257–272, 1992.

[PPS97] J. Picaut, J.D. Polack, and L. Simon. A mathematical diffuse field model based on a diffusion equation. *Acustica united with Acta Acustica*, 83:614–621, 1997.

[Reg61] T. Regge. General Relativity without Coordinates. *Il Nuovo Cimento*, XIX:558–571, Feb. 1961.

[Ste10] U.M. Stephenson. An energetic Approach for the Simulation of Diffraction within Ray Tracing Based on the Uncertainty Relation. *Acta Acustica united with Acustica*, 96:516–535, 2010.